AGU PUBLICATIONS

JGR

Journal of Geophysical Research: Atmospheres

RESEARCH ARTICLE
10.1002/2016JD025642

Key Points:
- New statistical approach, based on the unique spatiotemporal signature of FF emissions, can isolate and FF and biospheric emissions
- Robustly disaggregate FF fluxes regionally at monthly temporal resolution in winter months
- Covariance models and covariates based on temporally varying FF inventory data provide a more robust disaggregation over static proxies

Correspondence to:
V. Yadav,
vineet.yadav@jpl.nasa.gov

Citation:
Yadav, V., A. M. Michalak, J. Ray, and Y. P. Shiga (2016), A statistical approach for isolating fossil fuel emissions in atmospheric inverse problems, *J. Geophys. Res. Atmos.*, *121*, 12,490–12,504, doi:10.1002/2016JD025642.

Received 12 JUL 2016
Accepted 19 AUG 2016
Accepted article online 26 AUG 2016
Published online 18 OCT 2016

A statistical approach for isolating fossil fuel emissions in atmospheric inverse problems

Vineet Yadav[1,2], Anna M. Michalak[1], Jaideep Ray[3], and Yoichi P. Shiga[1,4]

[1]Jet Propulsion Laboratory, California Institute of Technology, Pasadena, California, USA, [2]Previously at Department of Global Ecology, Carnegie Institution for Science, Stanford, California, USA, [3]Sandia National Laboratories, Livermore, California, USA, [4]Department of Civil and Environmental Engineering, Stanford University, Stanford, California, USA

Abstract Independent verification and quantification of fossil fuel (FF) emissions constitutes a considerable scientific challenge. By coupling atmospheric observations of CO_2 with models of atmospheric transport, inverse models offer the possibility of overcoming this challenge. However, disaggregating the biospheric and FF flux components of terrestrial fluxes from CO_2 concentration measurements has proven to be difficult, due to observational and modeling limitations. In this study, we propose a statistical inverse modeling scheme for disaggregating winter time fluxes on the basis of their unique error covariances and covariates, where these covariances and covariates are representative of the underlying processes affecting FF and biospheric fluxes. The application of the method is demonstrated with one synthetic and two real data prototypical inversions by using in situ CO_2 measurements over North America. Inversions are performed only for the month of January, as predominance of biospheric CO_2 signal relative to FF CO_2 signal and observational limitations preclude disaggregation of the fluxes in other months. The quality of disaggregation is assessed primarily through examination of a posteriori covariance between disaggregated FF and biospheric fluxes at regional scales. Findings indicate that the proposed method is able to robustly disaggregate fluxes regionally at monthly temporal resolution with a posteriori cross covariance lower than 0.15 $\mu mol\, m^{-2}\, s^{-1}$ between FF and biospheric fluxes. Error covariance models and covariates based on temporally varying FF inventory data provide a more robust disaggregation over static proxies (e.g., nightlight intensity and population density). However, the synthetic data case study shows that disaggregation is possible even in absence of detailed temporally varying FF inventory data.

1. Introduction

The rising concentration of carbon dioxide (CO_2) in the atmosphere is the main driver of anthropogenic climate change. Spatial and temporal variations in global CO_2 fluxes leading to this increase can be inferred using inverse models from atmospheric observations that reflect the combined influence of fossil fuel (FF), biospheric, and oceanic fluxes. In inverse models, CO_2 concentration measurements are combined with atmospheric transport models driven by observed meteorology to yield estimates of the net exchange of CO_2 at the land and ocean surface [e.g., *Gurney et al*., 2002; *Michalak et al*., 2004; *Rayner et al*., 1999; *Tans et al*., 1990].

Recently, atmospheric inverse models have been proposed as a potential tool for independent verification of inventory-based estimates of FF fluxes or emissions. Such applications currently do not exist at regional (e.g., 1° by 1° and submonthly scale) to continental scales, due to the limitations associated with observational coverage [*Pacala et al*., 2010]. Improvements in terms of increasing in situ [e.g., *Sloop and Novakovskaia*, 2012] and satellite measurements [e.g., *Duren and Miller*, 2012] of CO_2 concentrations and in situ measurements of radiocarbon isotope ^{14}C [*Miller et al*., 2012] have been suggested as options toward reducing the uncertainty associated with continental and regional FF emissions estimates.

A variety of targeted efforts are ongoing for FF flux estimation at local to urban scales. Examples focusing on urban areas include the Megacities Carbon Project [*Duren and Miller*, 2012; *Gurney et al*., 2012; *Kort et al*., 2012] and the Indianapolis Flux Experiment (INFLUX) (http://influx.psu.edu/). At local scales (0.2–5 km) [*Christen*, 2014] the eddy covariance method has been employed to quantify FF emissions upwind from the location of the measurement tower [*Matese et al*., 2009; *Newman et al*., 2008; *Velazco et al*., 2011]. Estimation of FF fluxes and identification of its sources have also been attempted by studying upwind and downwind differences in the CO_2 mixing ratios along transects in urban and/or rural areas [*George et al*., 2007; *Gratani and*

Varone, 2005; *Idso et al*., 2001; *Mays et al*., 2009; *Rice and Bostrom*, 2011; *Rigby et al*., 2008]. Other urban studies have represented urban areas as boxes [*McKain et al*., 2012; *Kort et al*., 2012; *Turnbull et al*., 2015] with well-mixed boundary layer [see *Newman et al*., 2008; *Reid and Steyn*, 1997; *Strong et al*., 2011], whose height is determined by scattering of sound waves [e.g., *Zimnoch et al*., 2010] or through tracers like radon [e.g., *Vogel et al*., 2013], and fluxes are estimated by accounting for differences in upwind and downwind CO_2 concentrations [*Lauvaux et al*., 2013]. However, all these methods are extremely sensitive to the characterization of background concentrations, wind speed, boundary layer, and urban heat island (for details see *Cambaliza et al*. [2013]). Moreover, these methods do not scale to national or continental scales and can typically only be used to validate FF fluxes in urban areas.

Estimation of FF fluxes from inverse methods at continental scales requires disaggregation of biospheric and FF fluxes which has proven to be difficult due to seasonal variations in the contribution of these fluxes in determining total surface flux of CO_2 [*Shiga et al*., 2014]. Remote sensing of CO_2 has the capability to provide a large number of observations (for discussion on CO_2 observations from space, see *Crisp et al*. [2004] and *Olsen and Randerson*, [2004]) that can reduce the uncertainty of the FF fluxes estimated within an inverse modeling framework.

However, beyond an increase in observations, methodological improvements are also required in both transport and inverse models to realize the full potential of current and future CO_2 observations. In the case of inverse models, these methodological improvements include designing inverse modeling approaches that leverage the distinct statistical signatures of FF and biospheric fluxes in order to pinpoint their contributions to the total surface flux of CO_2.

To date, inversion efforts aimed at separating FF emissions from biospheric fluxes have relied on the use of isotopic tracers of FF CO_2 emissions [e.g., *Brioude et al*., 2012] to identify its contribution to the total CO_2 signal (for details on tracers of FF CO_2 see *Miller et al*. [2012]). However, a large fraction of the variance in FF fluxes remains unexplained by these tracers [*Miller et al*., 2012]. Studies that address the estimation of FF emissions over large spatial regions (compared to urban domes) are rare. In *Ray et al*. [2014a], the authors developed a parameterization of FF emission fields based on wavelets, and in *Ray et al*. [2014b] they use a sparse reconstruction method to estimate FF emissions using their spatial model in a synthetic data test case. Those methods were only applied within synthetic data experiments, however, and did not address the need to isolate FF emissions in the presence of biospheric fluxes. A study by *Shiga et al*. [2014], although not an inversion study per se, examined the degree to which concentration signatures specific to FF emissions were discernable from biospheric fluxes given (1) the current state of the atmospheric monitoring network in North America, (2) covariations between the seasonalities of variability in fluxes and atmospheric transport, and (3) limitations associated with contemporary atmospheric transport models. They found that outside of winter months, space-time patterns specific to FF emissions could not even be conclusively detected in observations of CO_2 from the North American monitoring network.

Here we hypothesize that for times and regions where the atmospheric monitoring network and atmospheric transport model provide, at a minimum, sufficient information to detect FF emissions, one could use the unique spatiotemporal features of FF fluxes to isolate them from confounding biospheric fluxes. To explore this idea, we present a geostatistical inverse modeling methodology that does not rely on FF tracers to separate FF and biospheric fluxes. Rather, the approach relies on (1) identifying spatially and temporally explicit covariates (variables correlated with FF emissions like night lights and population density) that provide some information about the space-time patterns of FF emissions and (2) isolating the covariance structure of the portion of the FF emissions patterns that cannot be captured by these covariates. A similar idea is applied to biospheric fluxes, with covariates and a covariance structure unique to the biospheric component of the total flux signal. Specifically, we treat easily observed proxies of FF and biospheric CO_2 fluxes as continuous predictors to construct a linear model for them; the models are then used within a geostatistical inverse formulation [e.g., *Michalak et al*., 2004; *Gourdji et al*., 2012; *Fang et al*., 2014]. The applicability of the proposed method is demonstrated within the context of one synthetic and two real data inversions at 1° spatial resolution for North America for the month of January 2008. In the synthetic data case study true fluxes are known in advance and are used to generate pseudo measurements. These measurements are then used to estimate fluxes. This allows direct comparison of the spatial distribution and magnitude of the true and estimated fluxes which is not possible in the real data case studies where true fluxes remain unknown.

The month of January is selected based on the analysis in *Shiga et al*. [2014] and the need to focus on a time when FF emissions are, at a minimum, detected given the limitations of the in situ monitoring network present in 2008 and atmospheric transport models. In these inversions the covariates and the error covariance model for biospheric fluxes are prescribed, whereas covariates and error covariance model for FF fluxes are chosen from a set of candidate covariates and error covariance models.

For more extensive applications, a method such as the one proposed here would need to be coupled with more widespread observational coverage provided by satellites and in situ measurement network, and ideally with improved atmospheric transport models.

2. Method for Flux Disaggregation

The process of disaggregating CO_2 fluxes is completed in two steps. First, the error covariance model and covariates for FF fluxes are selected using Bayesian Information Criterion (BIC; see section 2.4) and Restricted Maximum Likelihood (RML; see section 2.4) within geostatistical inverse modeling framework, after which in the second step, geostatistical inversions for separating FF and biospheric fluxes (see section 2.5.) are conducted. The quality of the separation of CO_2 fluxes is assessed, by examining a posteriori cross covariances between FF and biospheric fluxes.

2.1. Geostatistical Method for Separating Fossil Fuel and Biospheric Fluxes

A geostatistical formulation of the atmospheric inverse problem has been used to estimate biospheric CO_2 fluxes in several earlier studies [e.g., *Gourdji et al*., 2012; *Michalak et al*., 2004]. Unlike other Bayesian methods, this approach does not rely on prescribing prior fluxes; instead, it models the prior as a linear combination of a set of covariates with weights that are treated as hyperparameters ($\boldsymbol{\beta}$) and estimated as part of the inverse problem. Generally, covariates correlated with the flux are chosen to model the prior mean [e.g., *Gourdji et al*., 2008]. However, the approach also allows for the inclusion of covariates that are output from inventories and/or process-based models [e.g., *Fang et al*., 2014].

Under the assumption that the model-data mismatch can be modeled as a Gaussian distribution, the objective function for the standard geostatistical inverse model (GIM) can be written as

$$L_{\mathbf{s},\boldsymbol{\beta}} = (\mathbf{z} - \mathbf{H}\mathbf{s})^T \mathbf{R}^{-1} (\mathbf{z} - \mathbf{H}\mathbf{s}) + (\mathbf{s} - \mathbf{X}\boldsymbol{\beta})^T \mathbf{Q}^{-1} (\mathbf{s} - \mathbf{X}\boldsymbol{\beta}) \tag{1}$$

where $\mathbf{z}$ are measurements of CO_2 concentrations, $\mathbf{H}$ is a Jacobian matrix representing the sensitivity of measurements to underlying flux, $\mathbf{s}$ are the CO_2 fluxes, $\mathbf{R}$ is the model-data mismatch error covariance matrix, $\mathbf{X}$ is a matrix of covariates of $\mathbf{s}$, $\boldsymbol{\beta}$ are the coefficients or weights of individual covariates, and $\mathbf{Q}$ is the error covariance matrix describing the deviations of $\mathbf{s}$ from $\mathbf{X}\boldsymbol{\beta}$.

In this study, we modify this objective function to separately account for biospheric and FF fluxes. This modified objective function can be written as

$$\begin{aligned} L_{\mathbf{s}_{bio},\mathbf{s}_{ff},\boldsymbol{\beta}_{bio},\boldsymbol{\beta}_{ff}} \\ = (\mathbf{z} - [\mathbf{H}_{bio}\mathbf{s}_{bio} + \mathbf{H}_{ff}\mathbf{s}_{ff}])^T \mathbf{R}^{-1} (\mathbf{z} - [\mathbf{H}_{bio}\mathbf{s}_{bio} + \mathbf{H}_{ff}\mathbf{s}_{ff}]) \\ + (\mathbf{s}_{bio} - \mathbf{X}_{bio}\boldsymbol{\beta}_{bio})^T \mathbf{Q}_{bio}^{-1} (\mathbf{s}_{bio} - \mathbf{X}_{bio}\boldsymbol{\beta}_{bio}) \\ + (\mathbf{s}_{ff} - \mathbf{X}_{ff}\boldsymbol{\beta}_{ff})^T \mathbf{Q}_{ff}^{-1} (\mathbf{s}_{ff} - \mathbf{X}_{ff}\boldsymbol{\beta}_{ff}) \end{aligned} \tag{2}$$

where the subscripts *bio* and *ff* represent the biospheric and FF component of the terms defined in equation (1). This modified objective function embodies the assumptions that suitable covariates (in $\mathbf{X}$) and error covariance models ($\mathbf{Q}$) can be defined to statistically isolate FF and biospheric fluxes. Thus, the covariates ($\mathbf{X}_{bio}$, $\mathbf{X}_{ff}$) and error covariance models ($\mathbf{Q}_{bio}$,$\mathbf{Q}_{ff}$) in equation (2) play a vital role, as they capture our understanding of the processes affecting FF and biospheric flux variability. $\mathbf{H}_{bio}$ and $\mathbf{H}_{ff}$ in this study are based on the same atmospheric transport model but are kept separate to allow for the possibility of modeling $\mathbf{s}_{bio}$ and $\mathbf{s}_{ff}$ at different spatiotemporal resolutions.

The covariates and error covariance models in sections 2.2 and 2.3 are discussed specifically in the context of the three inversion case studies presented in this work. Other covariates and error covariance models could be implemented within equation (2), as needed for other applications.

2.2. Covariates and Error Covariance Model for Biospheric Fluxes

For the three inversion case studies presented here, the only covariates used for biospheric fluxes in $\mathbf{X}_{bio}$ are fixed effects that represent a 3-hourly diurnal cycle (see section 3 for details on the resolution of inversions). These covariates model the mean diurnal variations in the biospheric fluxes, and any spatiotemporal deviations therefrom are captured by the error covariance matrix $\mathbf{Q}_{bio}$. This choice of covariates for biospheric fluxes was made to focus primarily on evaluating the proposed method's ability to represent FF emissions.

Biospheric fluxes vary relatively smoothly, exhibit spatial autocorrelation, and are largely independent of FF fluxes. Thus, it is assumed for the inversion case studies that the error covariance for biospheric fluxes can be modeled through a stationary (for definition of stationarity, see *Cressie* [1993]) spatiotemporal exponential covariance model [see *Gourdji et al*., 2012]. This error covariance model can be written as (for details see *Gourdji et al*. [2010] and *Yadav and Michalak* [2013]

$$\mathbf{Q}_{bio} = \sigma^2 \left[\exp\left(\frac{-\mathbf{h}_{temporal_{bio}}}{l_{temporal_{bio}}} \right) \otimes \exp\left(\frac{-\mathbf{h}_{spatial_{bio}}}{l_{spatial_{bio}}} \right) \right] \tag{3}$$

where σ^2 is the variance in space and time, $\mathbf{h}_{spatial_{bio}}$ and $\mathbf{h}_{temporal_{bio}}$, are the separation distances between estimation locations of biospheric fluxes in space and time, and $l_{temporal_{bio}}$ and $l_{spatial_{bio}}$ are the spatial and temporal correlation range parameters and $\otimes$ denotes the Kronecker product. The three parameters σ^2, $l_{temporal_{bio}}$, and $l_{spatial_{bio}}$ of the spatiotemporal error covariance model are estimated through RML (see section 2.4 for details)

2.3. Covariates and Error Covariance Model for Fossil Fuel Fluxes

To aid in the disaggregation of FF fluxes from the biospheric fluxes, we include covariates that are correlated with FF fluxes in $\mathbf{X}_{ff}$. There are many easily available/observable proxies that correlate with FF fluxes, and we use the BIC [*Schwarz*, 1978] to select the smallest, most informative subset from a set of candidate proxies. This is described in detail in section 2.4. For the inversions presented here, the superset of candidate covariates of FF fluxes includes (1) annual radiance intensity of night lights at 3 km spatial resolution for 2008 [*Elvidge et al*., 1997], (2) annual population density per square kilometer at ~ 5 km spatial resolution for 2008 [*CIESIN*, 2012], (3) % built-up area at ~10 km spatial resolution for 2002 [*Miteva*, 2002], (4) percent urban area for 2009 [*Schneider et al*., 2009], and (5) a mixed, scaled estimate of FF fluxes of North America for 2008 from Vulcan and ODIAC (see section 3.1). All variables are aggregated up to the 1° spatial resolution for inversions.

Any spatiotemporal deviations from $\mathbf{X}_{ff}\boldsymbol{\beta}_{ff}$ are assumed to be independent and can thus be represented through a diagonal error covariance matrix with a different variance for each spatial location (i.e., each grid cell). This is consistent with the fact that FF fluxes estimated at 1° spatial resolution tend to be spatially localized (see section 3 for details on the spatial resolution of inversions).

The FF error covariance is thus defined here as

$$\mathbf{Q}_{ff} = \left(a \begin{bmatrix} k_1 & 0 & 0 \\ 0 & \ddots & 0 \\ 0 & 0 & k_r \end{bmatrix} + b \begin{bmatrix} 1 & 0 & 0 \\ 0 & \ddots & 0 \\ 0 & 0 & 1 \end{bmatrix} \right) \tag{4}$$

where a and b are constant variance components for all time periods for r spatial locations at which FF fluxes are estimated, and $k_1, \ldots, k_r$ define additional error variance that is spatially independent (i.e., the variance at each estimation location can be different).

We assume that the k_i values in equation (4) can be prescribed based on geospatial data sets related to FF fluxes, 10 of which are considered here. The first nine are the mean, maximum, and variance of night lights, population density, and percent built-up area within each $1° \times 1°$ grid cell in the inversion domain. These can be defined because all three of these data sets are available at higher resolution than the resolution of the inversions. The final data set considered is a FF inventory (Vulcan combined with ODIAC; see section 4) at the resolution of the inversions (see section 3 for details on the resolution of inversions), with this final dataset being temporally, as well as spatially, variable.

BIC is used to identify those geospatial data sets that most represent actual error covariances which are then used to populate the k_i values (see section 2.3). The primary objective is to obtain an optimal model that, in combination with covariates in $\mathbf{X}_{ff}$, can explain the spatiotemporal variability of FF fluxes.

2.4. Covariate and Covariance Selection From Bayesian Information Criterion

BIC evaluates the trade-off between the explanatory power of a model and its complexity. It is used for selecting an appropriate set of covariates from a superset of candidate covariates of the dependent variable. The set of covariates that forms the model with the lowest BIC value optimally balances explanatory power with model complexity. In this study, BIC is used to select covariates for both $\mathbf{X}_{ff}$ and $\mathbf{Q}_{ff}$. BIC is defined as

$$\mathrm{BIC} = \underbrace{\mathrm{RSS} + \ln|\boldsymbol{\Psi}|}_{\text{log likelihood}} + \underbrace{p\ln(n)}_{\text{penalty term}} \tag{5}$$

where $|\,|$ denotes the matrix determinant, p are the number of parameters or covariates in the model, and n is the number of observations.

RSS in equation (5) is defined as

$$\mathrm{RSS} = \left[\mathbf{z}^T\left(\boldsymbol{\Psi}^{-1} - \boldsymbol{\Psi}^{-1}\boldsymbol{\Omega}\left(\boldsymbol{\Omega}^T\boldsymbol{\Psi}^{-1}\boldsymbol{\Omega}\right)^{-1}\boldsymbol{\Omega}^T\boldsymbol{\Psi}^{-1}\right)\mathbf{z}\right] \tag{6}$$

where

$$\boldsymbol{\Psi} = [\,\mathbf{H}_{bio} \quad \mathbf{H}_{ff}\,]\begin{bmatrix}\mathbf{Q}_{bio} & 0\\ 0 & \mathbf{Q}_{ff}\end{bmatrix}[\,\mathbf{H}_{bio} \quad \mathbf{H}_{ff}\,]^T + \mathbf{R} \tag{7}$$

and

$$\boldsymbol{\Omega} = [\,\mathbf{H}_{bio} \quad \mathbf{H}_{ff}\,]\begin{bmatrix}\mathbf{X}_{bio}\\ \mathbf{X}_{ff}\end{bmatrix} \tag{8}$$

Note that BIC (equation (5)) depends on the covariance parameters in $\mathbf{Q}_{ff}$ (i.e., a and b), $\mathbf{Q}_{bio}$ (σ^2, $l_{temporal_{bio}}$, and $l_{spatial_{bio}}$) and $\mathbf{R}$ $\left(\sigma_R^2\right)$, which themselves depend on the covariates used to define $\mathbf{X}_{ff}$ and $\mathbf{Q}_{ff}$. The covariates and covariance parameters must therefore be adjusted in tandem to identify the overall best statistical model. We proceed as follows:

1. Pick one of the 10 covariates considered for populating the FF error covariance model ($\mathbf{Q}_{ff}$, equation (4)).
2. Use the discrete optimization branch and bound algorithm [see *Yadav et al*., 2013] and RML (for details see *Kitanidis* [1995]) to select covariates ($\mathbf{X}_{ff}$) and covariance parameters of $\mathbf{Q}_{ff}$, $\mathbf{Q}_{bio}$, and $\mathbf{R}$ (for estimates of covariance parameters of $\mathbf{Q}_{ff}$, $\mathbf{Q}_{bio}$ see Tables A1, A3a, and A3b) to simultaneously minimize BIC and the log likelihood of the expected value of the measurements ($\mathbf{z}$) with respect to a choice of a covariance model of $\mathbf{Q}_{ff}$ in step 1. This optimization procedure gives a set of covariates and covariance parameters associated with FF error covariance chosen in step 1.
3. Repeat steps 1 and 2 for each of the 10 different $\mathbf{Q}_{ff}$, i.e., FF error covariance models described in section 2.3
4. Compare BIC obtained in step 2 for all the 10 FF error covariance models and select the error covariance model that results in the minimum BIC.

2.5. Flux and A Posteriori Covariance Estimation

The FF and biospheric fluxes are estimated by solving linear system of equations (9) and (10) [e.g., *Michalak et al*., 2004], following which a posteriori covariance can be obtained from equation (11).

$$\begin{bmatrix}\boldsymbol{\Psi} & \boldsymbol{\Omega}\\ \boldsymbol{\Omega}^T & 0\end{bmatrix}\begin{bmatrix}[\,\boldsymbol{\Lambda}_{bio} \quad \boldsymbol{\Lambda}_{ff}\,]^T\\ \mathbf{M}\end{bmatrix} = \begin{bmatrix}[\,\mathbf{H}_{bio} \quad \mathbf{H}_{ff}\,]\begin{bmatrix}\mathbf{Q}_{bio} & 0\\ 0 & \mathbf{Q}_{ff}\end{bmatrix}\\ \begin{bmatrix}\mathbf{X}_{bio}\\ \mathbf{X}_{ff}\end{bmatrix}^T\end{bmatrix} \tag{9}$$

$$\begin{bmatrix}\hat{\mathbf{s}}_{bio}\\ \hat{\mathbf{s}}_{ff}\end{bmatrix} = [\,\boldsymbol{\Lambda}_{bio} \quad \boldsymbol{\Lambda}_{ff}\,]\mathbf{z} \tag{10}$$

$$\mathbf{V} = -\begin{bmatrix}\mathbf{X}_{bio}\\ \mathbf{X}_{ff}\end{bmatrix}\mathbf{M} + \begin{bmatrix}\mathbf{Q}_{bio} & 0\\ 0 & \mathbf{Q}_{ff}\end{bmatrix} - \begin{bmatrix}\mathbf{Q}_{bio} & 0\\ 0 & \mathbf{Q}_{ff}\end{bmatrix}[\,\mathbf{H}_{bio} \quad \mathbf{H}_{ff}\,]^T[\,\boldsymbol{\Lambda}_{bio} \quad \boldsymbol{\Lambda}_{ff}\,]^T \tag{11}$$

In equations (9)–(11), $\mathbf{V}$ is the a posteriori covariance of the estimated fluxes $\hat{\mathbf{s}}_{bio}$ and $\hat{\mathbf{s}}_{ff}$, $\boldsymbol{\Lambda}_{bio}$, and $\boldsymbol{\Lambda}_{ff}$ are the matrix of weights, $\mathbf{M}$ are Lagrange multipliers, and the remaining terms are as defined earlier. The posterior

covariance matrix **V** in equation (11) can be subdivided to represent the posterior covariances of the biospheric and FF fluxes, as well as their cross covariance, and can be given as

$$\mathbf{V} = \begin{bmatrix} \boldsymbol{V}_{bio} & \boldsymbol{V}_{ff,bio}^{T} \\ \boldsymbol{V}_{ff,bio} & \boldsymbol{V}_{ff} \end{bmatrix} \tag{12}$$

where $\boldsymbol{V}_{bio}$, $\boldsymbol{V}_{ff}$ represent posterior covariance of estimated biospheric and FF fluxes and $\boldsymbol{V}_{ff,bio}$ represent their cross covariance.

2.6. Nonnegativity Constraints on Fossil Fuel Fluxes

The joint inversion can result in negative FF fluxes, and therefore, a nonnegativity constraint is imposed on the FF fluxes obtained from equation (10). No constraints are imposed on $\hat{\mathbf{s}}_{bio}$, $\widehat{\boldsymbol{\beta}}_{bio}$, and $\widehat{\boldsymbol{\beta}}_{ff}$ as they admit both negative and positive values. There are several methods for imposing nonnegativity constraints on $\hat{\mathbf{s}}_{ff}$ [e.g., *Miller et al*., 2014]. However, some of these methods do not scale to large dimensional inverse problems, while others make the problem nonlinear. Consequently, we used Lagrange multipliers as a mechanism for implementing the nonnegativity constraints. This method consists of rewriting the original objective function given in equation (2) into a Lagrangian formulation [e.g., *Michalak and Kitanidis*, 2003]:

$$h\left(L_{\mathbf{s}_{bio},\mathbf{s}_{ff},\boldsymbol{\beta}_{bio},\boldsymbol{\beta}_{ff}},\boldsymbol{\lambda}\right) = f\left(L_{\mathbf{s}_{bio},\mathbf{s}_{ff},\boldsymbol{\beta}_{bio},\boldsymbol{\beta}_{ff}}\right) - \sum_{i=1}^{t} \lambda_i \left[\delta_i(\mathbf{s}_{ff}) - b_i\right] \tag{13}$$

where t values are the total number of active constraints and $\boldsymbol{\lambda} = (\lambda_1, \lambda_1, \ldots, \lambda_p)$ are the Lagrange multipliers and $L_{\mathbf{s}_{bio},\mathbf{s}_{ff},\boldsymbol{\beta}_{bio},\boldsymbol{\beta}_{ff}}$ must satisfy the constraints such that $\boldsymbol{\delta}_i(\mathbf{s}_{ff}) \geq \boldsymbol{b}_i$. This involves setting the derivative of the Lagrange function equal to zero by satisfying the first order Kuhn-Tucker conditions (for additional details, see *Gill et al*. [1981]). Note that nonnegativity constraints are imposed on FF fluxes obtained from an unconstrained inversion that utilizes the covariance model and covariates selected from the procedure described in section 2.4. While imposing nonnegativity $\hat{\mathbf{s}}_{bio}$, $\hat{\mathbf{s}}_{ff}$, $\widehat{\boldsymbol{\beta}}_{bio}$, and $\widehat{\boldsymbol{\beta}}_{ff}$ are updated in each iteration, the a posteriori covariance is not updated and the uncertainty reported in section 4 is obtained from the first inversion where nonnegativity constraints are not imposed.

3. Inversion Case Studies

Three inversion case studies are used to evaluate the proposed approach. All involve estimating biospheric fluxes at 3-hourly temporal resolution to avoid temporal aggregation errors (for details see *Gourdji et al*. [2010]), while FF fluxes are estimated at 8 day temporal resolution, in part due to the computational cost of imposing nonnegativity constraints. Spatially, both FF and biospheric fluxes are estimated at 1° by 1° for the land area between 10°N to 70°N and 50°W to 170°W. All inversions are conducted for January 2008.

3.1. Data for Inversion Case Studies

The sensitivity matrix (**H**) of the CO_2 observations to surface fluxes for inversions was obtained from Weather Research Forecasting model-Stochastic Time-Inverted Lagrangian Transport (STILT) [*Lin et al*., 2003] model that has been utilized in many studies for estimating fluxes (for details see *Gourdji et al*. [2012] and *Shiga et al*. [2014]).

For two real data case studies continuous measurements of atmospheric CO_2 concentrations from 29 in situ towers across North America were used. These 29 towers include (1) nine towers operated by the Global Monitoring Division of NOAA's Earth Research Laboratory [*Andrews et al*., 2015], located in Park Falls, Wisconsin (LEF); Moody, Texas (WKT); West Branch, Iowa (WBI); Boulder Atmospheric Observatory, Colorado (BAO); Argyle, Maine (AMT); South Carolina Tower, South Carolina (SCT), and Walnut Grove, California (WGC); Shenandoah National Park, Virginia (SNP); and Barrow, Alaska (BRW); (2) seven towers supported by the Mid-Continental Intensive project, located in Canaan Valley, West Virginia (CVA); Missouri Ozarks, Missouri (OZA) [*Stephens et al*., 2011]; Kewanee, Illinois (KEW); Centerville, Iowa (CEN); Mead, Nebraska (MEA); Round Lake, Missouri (ROL); and Galesville, Wisconsin (GAL) [*Richardson et al*., 2012]; (3) three towers within the Regional Atmospheric Continuous CO_2 Network in the Rocky Mountains (RACCOON) [*Stephens et al*., 2011], located in Storm Peak Lab, Colorado (SPL); Niwot Ridge, Colorado (NWR); and Hidden Peak Snowbird, Utah (HDP); (4) seven towers supported by Environment Canada, located in Fraserdale, Ontario (FRD); Egbert, Ontario (EGB); Candle Lake, Saskatcheway (CDL); East Trout Lake,

Saskatchewan (ETL); Sable Island, Nova Scotia (SBL); Lac LaBiche, Alberta (LLB); and Chibougamau, Quebec (CHI); (5) five Oregon towers operated by Oregon State University [*Göckede et al*., 2010], including the Fir (FIR), Metolius (MET), Yaquina Head (YAH), Mary's Peak (MAP), and Burns Old (NGB); and (6) four additional towers, located at the Harvard Forest, Massachusetts (HFM) [*Urbanski et al*., 2007]; Morgan Monroe State Forest, Illinois (MMS) [*Dragoni et al*., 2007; *Schmid et al*., 2000]; Southern Great Plains, Oklahoma (SGP); and La Jolla, CA (LJA) [*Keeling et al*., 2005].

We use ~2400 3 hr average CO_2 observations that have been filtered and processed as in *Fang et al.* [2014] for use in inverse modeling applications by removing anomalous data due to low-quality flags, extreme outliers, large deviations (±30 ppm) from the background, possible transport model concerns, and ocean sensitivity. Additionally, we remove the influence of boundary conditions from the atmospheric measurements as in *Fang et al*. [2014]. The names, locations, and measurement times of the CO_2 observations are given in Table A1.

In the synthetic data case study, the "ground truth" for biospheric fluxes was obtained from the Carnegie Ames Stanford Approach (CASA) model as configured for the Global Fire Emissions Database (GFED) v2 project [*Randerson et al*., 1997; *van der Werf et al*., 2006]. These simulated fluxes were obtained from model runs submitted to the North American Carbon Program Regional Interim Synthesis (for details see *Huntzinger et al*. [2012]). The estimates for FF fluxes were obtained from the Vulcan (USA; 2002) and ODIAC (Canada, Mexico and Alaska; 2007) inventories [*Gurney et al*., 2009; *Oda and Maksyutov*, 2011]. These were then scaled to 2008 to account for changes in the FF fluxes from those reported in these inventories. Since the CASA-GFED v2 biospheric fluxes were available only at monthly scale they were downscaled to 3-hourly temporal resolution by using net shortwave radiation and near-surface temperature data from the NASA Global Land Data Assimilation System (GLDAS) [*Olsen and Randerson*, 2004; *Rodell et al*., 2004]. Finally, synthetic observations were generated by adding (1) the estimates of FF fluxes from Vulcan and ODIAC and (2) biospheric fluxes from CASA-GFED v2 model at 3-hourly resolution and transporting them forward (e.g., $[\mathbf{H}_{bio} \quad \mathbf{H}_{ff}]$ $(\mathbf{s}_{ff} + \mathbf{s}_{bio})$) through sensitivity matrix $[\mathbf{H}_{bio} \quad \mathbf{H}_{ff}]$.

3.2. Real Data Case Studies

The real data case studies were designed to test the influence of a FF inventory in explaining variations in inferred FF fluxes and disaggregating them from biospheric fluxes. This is achieved by examining a posteriori cross covariances and results of the model selection. Thus, in one case study, the model selection scheme (see section 2.4) is allowed to select covariates and an error covariance model for FF fluxes from the full superset given in section 2.3 (henceforth RD1), whereas in the second case study this superset excludes covariate and error covariance model based on FF inventory (henceforth RD2). This distinction was made to explore the additional error/uncertainty incurred due to the lack of a detailed inventory, a realistic constraint in many parts of the world.

3.3. Synthetic Data Case Study

The goal of the synthetic data case study (henceforth SD) was to evaluate the performance of the inversion method when true fluxes are known. Its results provide a two-way indication of the performance of the proposed method in disaggregating fluxes, that is, (1) through analysis of a posteriori cross covariance between FF and biospheric fluxes and (2) through comparison of the estimated fluxes with true fluxes (see section 4). Overall, this case study is similar to the RD2, as FF inventory estimates are not used as candidate covariates in $\mathbf{X}_{ff}$ or $\mathbf{Q}_{ff}$. This is because in this case the synthetic CO_2 observations are themselves generated using inventory data sets, and using this same data set in the inversion would have provided an unrealistic amount of information about the true fluxes to the inversion. A zero-mean Gaussian white noise with variances equal to those in the model-data mismatch matrix ($\mathbf{R}$) in RD2 was added to the synthetic CO_2 observations. $\mathbf{R}$ in SD is fixed to equal that in RD2, whereas the $\mathbf{Q}_{ff}$ and $\mathbf{Q}_{bio}$ covariance parameters and covariates are obtained from the procedure described in section 2.4. The quality of disaggregation is examined by comparing the inferred fluxes with the true fluxes, i.e., CASA-GFED v2 biospheric and Vulcan and ODIAC FF fluxes.

3.4. Framework for Evaluating Case Studies

The Frobenius norm (for description see *Golub and Van Loan* [2012]) of FF and biospheric a posteriori cross covariances is computed to check for the quality of the separation of the estimated fluxes. To compute the

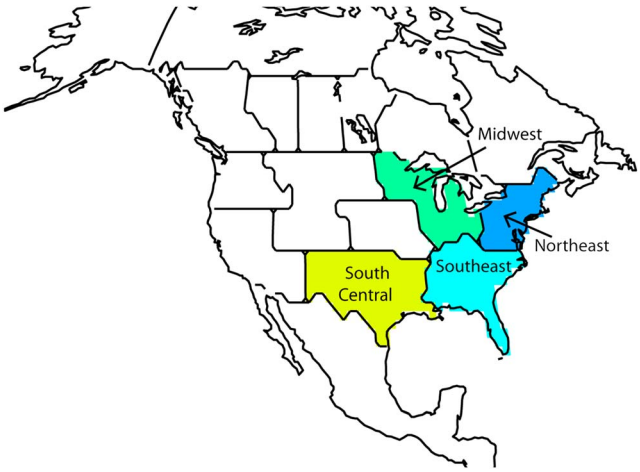

Figure 1. Regional classification map for aggregating fluxes and a posteriori cross covariances of biospheric and fossil fuel fluxes.

Frobenius norm of cross covariances, the a posteriori covariances are first aggregated temporally to monthly resolution at grid scale to evaluate the degree to which biospheric and FF fluxes can be isolated at timescales relevant for understanding carbon budgets.

This monthly covariance is obtained through the law of the sum of the variance of random variables in space and time and can be written as

$$\overline{\mathbf{V}} = \begin{bmatrix} \overline{\boldsymbol{V}}_{bio} & \overline{\boldsymbol{V}}_{ff,bio}^{T} \\ \overline{\boldsymbol{V}}_{ff,bio} & \overline{\boldsymbol{V}}_{ff} \end{bmatrix} \tag{14}$$

where $\overline{\mathbf{V}}$ is a posteriori covariance of the fluxes aggregated to monthly temporal resolution, $\overline{\boldsymbol{V}}_{bio}$ and $\overline{\boldsymbol{V}}_{ff}$ are a posteriori covariances of the biospheric and FF fluxes at monthly resolution, respectively, and $\overline{\boldsymbol{V}}_{ff,bio}$ represents their cross covariance. The Frobenius norm for $\overline{\boldsymbol{V}}_{ff,bio}$ is computed as

$$\left\|\overline{\boldsymbol{V}}_{ff,bio}\right\|_{F} = \sqrt{\text{Trace}\left(\overline{\boldsymbol{V}}_{ff,bio}^{T}\overline{\boldsymbol{V}}_{ff,bio}\right)} \tag{15}$$

where $\|\ \|$ stands for the norm and all other terms are as defined earlier. A smaller Frobenius norm of $\overline{\boldsymbol{V}}_{ff,bio}$ indicates better separation of the two signals and low a posteriori cross covariance between the disaggregated fluxes.

The model resolution matrix of the estimated FF fluxes at the 8 day temporal resolution was also examined. The model resolution matrix indicates the quality of estimated fluxes and can be given as

$$\hat{\mathbf{m}}_{ff} = \boldsymbol{\Lambda}_{ff}^{T}\mathbf{H}_{ff} \tag{16}$$

where $\hat{\mathbf{m}}_{ff}$ is the model resolution matrix and all other terms are as described earlier. The quality of the estimated FF fluxes is assessed by computing the ℓ^2 norm of $\hat{\mathbf{m}}_{ff}$. A ℓ^2 norm of 1 of $\hat{\mathbf{m}}_{ff}$ indicates that estimated FF fluxes can be independently determined, whereas a value greater than 1 indicates that only average fluxes can be determined, with progressively larger ℓ^2 norms indicating progressively poor estimation of FF fluxes (for details see *Menke* [2013]).

The correlation between true and modeled concentration was also examined for the two real data case studies.

4. Results and Discussion

The quantification of fossil fuel emissions from atmospheric observations depends on the availability of an observational network that is sufficiently sensitive to FF emissions and the methodological framework for isolating the biospheric and FF components of the terrestrial fluxes. An approach for fulfilling the second of these needs is presented here. This approach is evaluated within four regions of the United States (Figure 1), because these are the regions for which the observational network in 2008 was relatively more effective at detecting FF emissions [*Shiga et al.*, 2014].

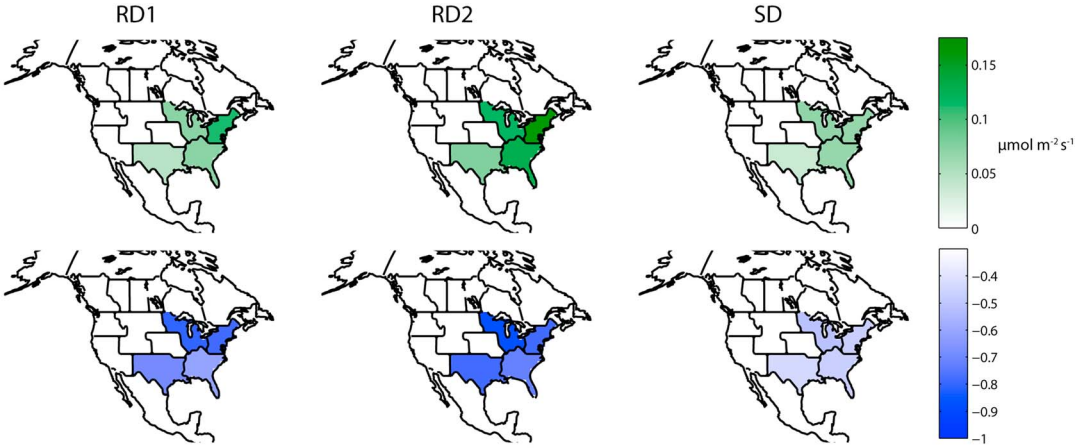

Figure 2. Row 1 represents the a posteriori cross covariances (shown here is square root of the absolute value of the cross covariance $\left(\overline{\boldsymbol{V}}_{\mathrm{ff,bio}}\right)$, so that it is comparable to the uncertainty bounds from Figures 3 and 4.) of the FF and biospheric fluxes, aggregated a posteriori to monthly temporal resolution and regional spatial scale for the three case studies. Row 2 shows the correlation coefficients of these a posteriori uncertainties. Smaller covariances and correlation coefficients imply better separation between fossil fuel and biospheric flux estimates.

For the RD1 case study, the fossil fuel inventory is selected both as the spatial trend of the FF emissions ($\mathbf{X}_{ff}$), and as the data set used to populate the error covariance matrix ($\mathbf{Q}_{ff}$). Intuitively, in the context of the inversion case studies, the choice of a FF trend and error covariance model selected by BIC implies that among all candidate models it is best suited for (1) describing the variance in the spatial distribution of FF emissions, (2) identifying the FF signal in the CO_2 observations, (3) separating FF and biospheric fluxes, and (4) computing estimates of FF and biospheric fluxes. The selection of the FF inventory by BIC in the RD1 case is not a surprise, as this inventory is indeed expected to be more representative of the true FF emissions patterns relative to the other candidate variables. Moreover, it also shows that covariates of FF emissions with high spatiotemporal resolution (e.g., diurnally and seasonally varying) are more representative of the true distribution of FF fluxes relative to covariates that do not vary in time (e.g., urban areas). Covariates of FF fluxes that typically vary at daily temporal resolution were included in this study, but they did not have any temporal variability as we did not have access to these data (e.g., Landscan population density data) or due to nonavailability of data at this temporal resolution (e.g., night lights).

Results from RD1 confirm that the statistical framework presented here can be used to disaggregate biospheric and FF terrestrial CO_2 fluxes when observations are sufficiently sensitive to FF emissions. The success of the disaggregation of FF and biospheric fluxes in RD1 can be evaluated by examining the a posteriori cross covariance and cross correlation of uncertainties (Figure 2; also see Table A2) between these component flux estimates at aggregated spatial (i.e., regional) and temporal (i.e., monthly) scales. The cross covariances are generally small relative to the magnitude of the fluxes (Figure 2), and the cross correlations are low, except for the Midwest.

An inversion was also performed for July (results not shown) for all three case studies. This was done to test our ability to disaggregate FF fluxes from biospheric fluxes in a summer month. We found that both ℓ^2 and

Table 1. Covariates and Error Covariance Models Selected by BIC for $\mathbf{X}_{ff}$ and $\mathbf{Q}_{ff}$ for the Three Case Studies

	Covariates							
Case Studies	Mean Night Light Intensity	Mean Population Density	Percent Built-Up Area	Percent Urban Area	FF Inventory	FF Covariance Model	Frobenius Norm $(\mu\mathrm{mol\,m^{-2}\,s^{-1}})^2$	ℓ^2 Norm of Model Resolution Matrix
RD1					✓	Mean (FF inventory)	6.92	2.53
RD2		✓		✓	N/A	Maximum (night lights intensity)	9.69	4.86
SD	✓	✓			N/A	Variance (population density; per square kilometer)	6.95	3.53

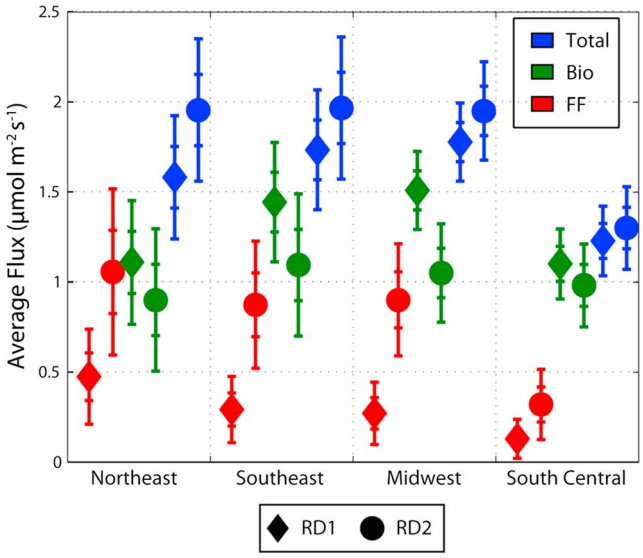

Figure 3. Estimates of the fossil fuel, biospheric, and total flux with one standard deviation (first hash mark) and two standard deviation uncertainty bounds for the regions shown in Figure 1 for the two real data case studies. Diamonds represent RD1; circles represent RD2.

Frobenius norm for January (equation (15) and Table 1) was over a factor of 15 times lower than those obtained for July and fossil fuel emissions were not detectable by the measurement network due to the large confounding influence of the biospheric fluxes (see also *Shiga et al.* [2014]). The small Frobenius norm in January is another indication of the small cross covariances between the FF and biospheric flux uncertainties. This is further confirmed by the ℓ^2 norm of the model resolution matrix (see equation (16) and Table 1) and the coefficient of determination of 0.84 (see Figure A1) between the true and posteriori fit of observations obtained by transporting forward the estimated fluxes for the month of January 2008.

For the RD2 case study, the fossil fuel inventory is made unavailable for the variable selection (for both the trend ($\mathbf{X}_{ff}$) and prior error covariance ($\mathbf{Q}_{ff}$) models). This leads to the selection of mean population density, percent urban land cover ($\mathbf{X}_{ff}$) and the maximum value of night lights intensity ($\mathbf{Q}_{ff}$) as alternatives (Table 1). The impact of using these data sets, which are less directly representative of the underlying FF emissions, is seen via increased cross covariances (Figure 2) and cross correlations in the monthly regional posterior uncertainties of the biospheric and FF fluxes in the RD2 case study. The Frobenius norm, ℓ^2 norm (Table 1), and correlation between true and posterior fit of observations (Figure A1) as in RD1 is low and the estimates of total fluxes (Figure 3) show similar uncertainties on the total flux relative to RD1 (Figure 3) but increased uncertainties on the component contributions from FF and biospheric fluxes.

For the SD case study, the fossil fuel inventory is also made unavailable for the variable selection, as it is used to create the synthetic observations. The selected alternate covariates are night light intensity and population density ($\mathbf{X}_{ff}$) and the variance of population density within each 1° by 1° grid cells ($\mathbf{Q}_{ff}$) (Table 1). These are different from the ones selected in RD2. This is due to the differences between the RD and SD setups, including the nature of the true FF fluxes and the impact of transport model errors. The effect of using these data sets, which are proxies of FF emissions, on the posterior cross covariances and cross correlations (Figure 2) in the biospheric and FF uncertainties is similar to that observed in RD2, though with a lower Frobenius norm of $\overline{\boldsymbol{V}}_{ff,bio}$ relative to RD2 case study.

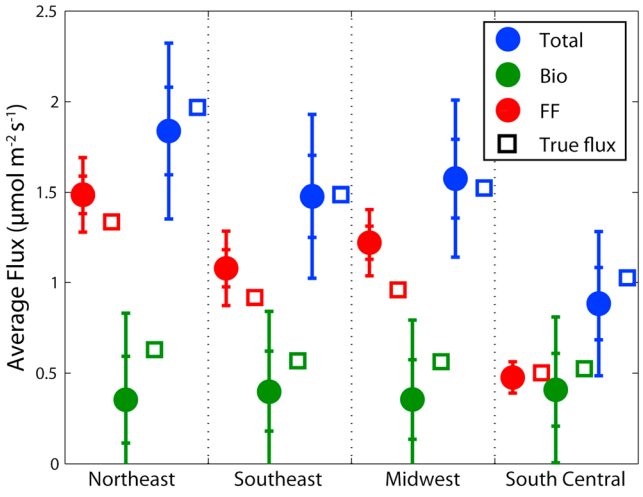

Figure 4. Estimates of fossil fuel, biospheric, and total fluxes with one standard deviation (first hash mark) and two standard deviation uncertainty bounds for the regions shown in Figure 1 for the synthetic data case.

For the SD case study, the FF, biospheric, and total fluxes can also be compared to their "true" values (Figure 4). Results confirm that although the separation of FF and biospheric flux become more

Table A1. Locations and Measurement Times of CO_2 Concentrations Across Study Sites (In Situ Towers)[a]

Tower	Name	Latitude	Longitude	Time of Day (Local Time, h)	Height (m)	RD1σ_R (ppm)	RD2σ_R (ppm)
LEF	Park Falls	45.95	−90.27	1 4 7 10 13 16 19 22	396	1.49	1.41
WKT	Moody	31.32	−97.33	1 4 7 13 16 19 22	457	1.18	1.16
WBI	West Branch	41.73	−91.35	1 4 7 10 13 16 19 22	379	1.16	1.13
BAO	Boulder Observatory	40.05	−105.01	1 4 7 13 16 19 22	300	1.59	1.59
WGC	Walnut Grove	38.27	−121.49	1 4 7 13 16 19 22	483	5.39	5.34
AMT	Argyle	45.03	−68.68	13 16 19	107	2.99	2.84
BRW	Barrow	71.32	−156.61	1 4 7 10 13 16 19 22	17	0.01	0.09
FRD	Fraserdale	49.88	−81.57	13 16 19	40	2.64	0.56
CDL	Candle Lake	53.99	−105.12	13 16 19	30	1.56	0.58
SBL	Sable Island	43.93	−60.02	1 4 7 10 13 16 19 22	25	1.36	1.36
EGB	Egbert	44.23	−79.78	13	3	3.99	4.03
ETL	East Trout Lake	54.35	−104.99	10 13 16 19	105	3.35	0.86
LLB	Lac LaBiche	54.95	−112.45	13	10	3.03	2.99
CHI	Chibougamau	49.69	−74.34	13 16 19	30	0.48	0.47
HFM	Harvard Forest	42.54	−72.17	13 16 19	30	3.13	3.20
ARM	Southern Great Plains	36.8	−97.5	13 16 19	60	1.26	1.23
MOM	Morgan Monroe	39.32	−86.41	13 16 19	48	4.64	4.79
OZA	Ozark	38.74	−92.2	13 16 19	30	0.97	0.95
KEW	Kewanee	41.28	−89.97	13 16 19	140	1.95	1.88
CEN	Centerville	40.79	−92.88	13 16 19	110	0.90	0.91
MEA	Mead	41.14	−96.46	13 16 19	122	0.63	0.48
ROL	Round Lake	43.53	−95.41	13 16 19	110	1.14	1.04
GAL	Galesville	44.09	−91.34	13 16 19	122	2.02	2.03
NWR	Niwot Ridge	40.05	−105.58	1	5	2.2	1.21
HDP	Hidden Peak Snowbird	40.56	−111.65	1	18	0.82	0.81
FIR	Fir	44.65	−123.55	13 16 19	38	3.26	3.22
MET	Metolius	44.45	−121.56	13 16 19	34	0.65	0.61
YAH	Yaquina Head	44.67	−124.07	13 16 19	13	2.08	2.05
NGB	NGBER	43.47	−119.69	13 16 19	7	1.07	1.06

[a]Modified (removed sites with no data in January 2008) from *Shiga et al.* [2014]; see Table S1 in *Shiga et al.* [2014]). Note that the variances or model-data mismatch (σ_R) are obtained a priori through Restricted Maximum Likelihood, from the method described in section 2.4.

Table A2. Metrics Computed From A Posteriori Covariances for Regions Shown in Figure 1[a]

	RD1	RD2	SD
A Posteriori Correlation Coefficient Between Biospheric and Fossil Fuel Fluxes			
Northeast	−0.55	−0.56	−0.19
Southeast	−0.35	−0.48	−0.19
Midwest	−0.58	−0.66	−0.24
South central	−0.44	−0.55	−0.16
A Posteriori Cross Covariance Between Biospheric and Fossil Fuel Fluxes ($\mu mol\, m^{-2}\, s^{-1})^2$			
Northeast	−0.012	−0.026	−0.005
Southeast	−0.005	−0.017	−0.004
Midwest	−0.005	−0.014	−0.005
South central	−0.002	−0.006	−0.001
A Posteriori Standard Deviation of Fossil Fuel Fluxes ($\mu mol\, m^{-2}\, s^{-1}$)			
Northeast	0.132	0.231	0.103
Southeast	0.092	0.176	0.103
Midwest	0.087	0.155	0.092
South central	0.054	0.098	0.044
A Posteriori Standard Deviation of Biospheric Fluxes ($\mu mol\, m^{-2}\, s^{-1}$)			
Northeast	0.171	0.197	0.240
Southeast	0.166	0.197	0.222
Midwest	0.109	0.136	0.220
South central	0.097	0.115	0.201

[a]Note that a posteriori cross-correlation coefficients and cross covariances have also been shown in Figure 2. Correlation coefficients shown in Figure 2 are computed by dividing the a posteriori cross covariances by the product of a posteriori standard deviations of the biospheric and fossil fuel fluxes.

Table A3a. Estimates for $\mathbf{Q}_{bio}$ Covariance Parameters for Three Case Studies[a]

Case Studies	σ (μmol m^{-2} s^{-1})	$l_{temporal_{bio}}$ (days)	$l_{spatial_{bio}}$ (km)
RD1	5.15	2.69	400
RD2	5.71	3.20	383
SD	0.21	5.28	1204

[a]Note that only results for the fossil fuel covariance structure that minimized BIC (see Table 1) are shown. Estimates for $\mathbf{Q}_{bio}$ covariance parameters for three case studies.

uncertain in the absence of a good inventory, the separation is still relatively robust, in the sense that the true fluxes lie within the range of the posterior uncertainties. The poorest performance is in the Midwest, which is also the region with the highest cross covariance and cross correlation in the posterior uncertainties. Another indication of the good overall performance of the flux disaggregation is the low RMSE of the 1° by 1° fluxes at the native temporal resolution of the inversion (3-hourly for biospheric fluxes, 8 day for FF fluxes), namely, 0.33 μmol m^2 s^{-1} for FF emissions and 0.22 μmol m^2 s^{-1} for biospheric fluxes, relative to the magnitude of the fluxes (Figure 4).

5. Conclusions

With increasing attention being placed on accurate monitoring of FF emissions, the ability to provide a top-down verification of inventory-based estimates of FF emissions, by disaggregating FF and biospheric fluxes, is a promising development. The sparsity of in situ measurement networks, the small relative contribution of FF flux to the total observed CO_2 fluctuations, especially during the growing season and the large model-data mismatch errors due, in large part, to uncertainties associated with modeling of atmospheric transport severely limit the ability of inverse models to accurately estimate FF emissions.

Assuming that there is low systematic bias in WRF-STILT transport model, the analyses described in this paper demonstrate that the proposed method is successful in separating FF and biospheric fluxes at subcontinental scales. This confirms the potential of using a statistical approach, based on the unique spatiotemporal signature of FF emissions, to isolate and estimate FF emissions using CO_2 observations.

Our method performs the disaggregation of biospheric and FF CO_2 emissions using error covariance models and flux covariates (e.g., night lights and population density) that are specific to biospheric and FF fluxes. These models and covariates are quite different for the two flux components and are fundamental to a successful disaggregation. We find that using a FF inventory to construct an error covariance model for FF fluxes provides a better disaggregation relative to the case when static proxies of FF fluxes are used. This is due to the better spatiotemporal fidelity that an inventory provides to the FF fluxes being estimated, relative to the other proxies. The synthetic data case study shows that even in the absence of a detailed FF inventory, other static FF-related variables can provide sufficient information to adequately disaggregate and estimate FF and biospheric fluxes.

In both cases, the ability to disaggregate flux components is predicated on the availability of a monitoring network that is sufficiently sensitive to both types of fluxes. The addition of column-averaged dry air mole fraction observations [*Kuai et al*., 2013] from satellites (for list of satellites that measure CO_2 see *Kulawik et al*. [2013]) and tracers that provide independent information on FF emissions would undoubtedly further improve the FF emission estimates.

The ability to accurately disaggregate and estimate FF and biospheric fluxes using atmospheric data is a continuing challenge. This pursuit relies heavily on external conditions including, but not limited, to the representativeness and density of the observational network as well as transport model accuracy. Nevertheless, the methodological advances presented here, specifically the exploitation of the unique spatiotemporal structure of FF emissions, offers an approach to optimally leverage the information content of available data to provide a complementary approach for estimating FF fluxes.

Table A3b. Estimates for $\mathbf{Q}_{ff}$ Covariance Parameters for Three Case Studies[a]

Case Studies	a (μmol m^{-2} s^{-1})	b (unitless)
RD1	0.02	8.69E−8
RD2	2.33	4.62E−13
SD	1.01E−6	6.0E−3

[a]Note that only results for the fossil fuel covariance structure that minimized BIC (see Table 1) are shown. Estimates for $\mathbf{Q}_{bio}$ covariance parameters for three case studies.

Acknowledgments
This work was supported by Sandia National Laboratories' LDRD (Laboratory Directed Research and Development) funds, sponsored by the Geosciences Investment Area. Sandia National Laboratories is a multiprogram laboratory managed and operated by Sandia Corporation, a wholly owned subsidiary of Lockheed Martin Corporation, for the U.S. Department of Energy's National Nuclear Security Administration under contract DE-AC04-94AL85000. Additional funding for this research came from National Science Foundation under grant 1342076. Some of this research, was carried out at the Jet Propulsion Laboratory, California Institute of Technology, under a contract NNN15R040T between Carnegie Institution of Washington and National Aeronautics and Space Administration. We gratefully acknowledge the efforts of the PIs of the various towers providing continuous atmospheric CO_2 observations, which were instrumental for these analyses. The sites BRW, WGC, SNP, SCT, AMT, WBI, BAO, LEF, and WKT are part of NOAA's Global Greenhouse Gas Reference Network operated by the Global Monitoring Division of NOAA's Earth System Research Laboratory with additional support from NOAA's Climate Program Office and are a contribution to the North American Carbon Program. The installation of CO_2 sampling equipment was made possible at AMT, by a grant from the National Science Foundation Biocomplexity in the Environment Program (ATM-0221850), at SNP, by the University of Virginia, and at SCT by funding provided by the DOE Office of Science–Terrestrial Carbon Processes program. The Savannah River National Laboratory (SRNL) provided support during the installation at SCT and provides ongoing support via funding from NOAA. SNRL is operated by Savannah River Nuclear Solutions, LLC, under contract DE-AC09-08SR22470 with the U.S. Department of Energy. WGC measurements were supported by a combination of the California Energy Commission's Public Interest Environmental Research Program to the Lawrence Berkeley National Laboratory under contract DE-AC02-05CH11231 and NOAA. Research at CVA, OZA, KEW, CEN, MEA, ROL, and GAL was sponsored by the U.S. Department of Energy Office of Science TCP program (DE-FG02-06ER64315) and by the U.S. Department of Commerce, NOAA office of Global Programs (NA08OAR4310533). The five Oregon sites FIR, MET, YAH, MAP, and NGB were supported by NOAA (NA11OAR4310056). The research at the MMS site was sponsored by the U.S.

Appendix A

Scatterplot of true and posterior concentration fits for two real data case studies after removing the influence of inflow of CO_2.

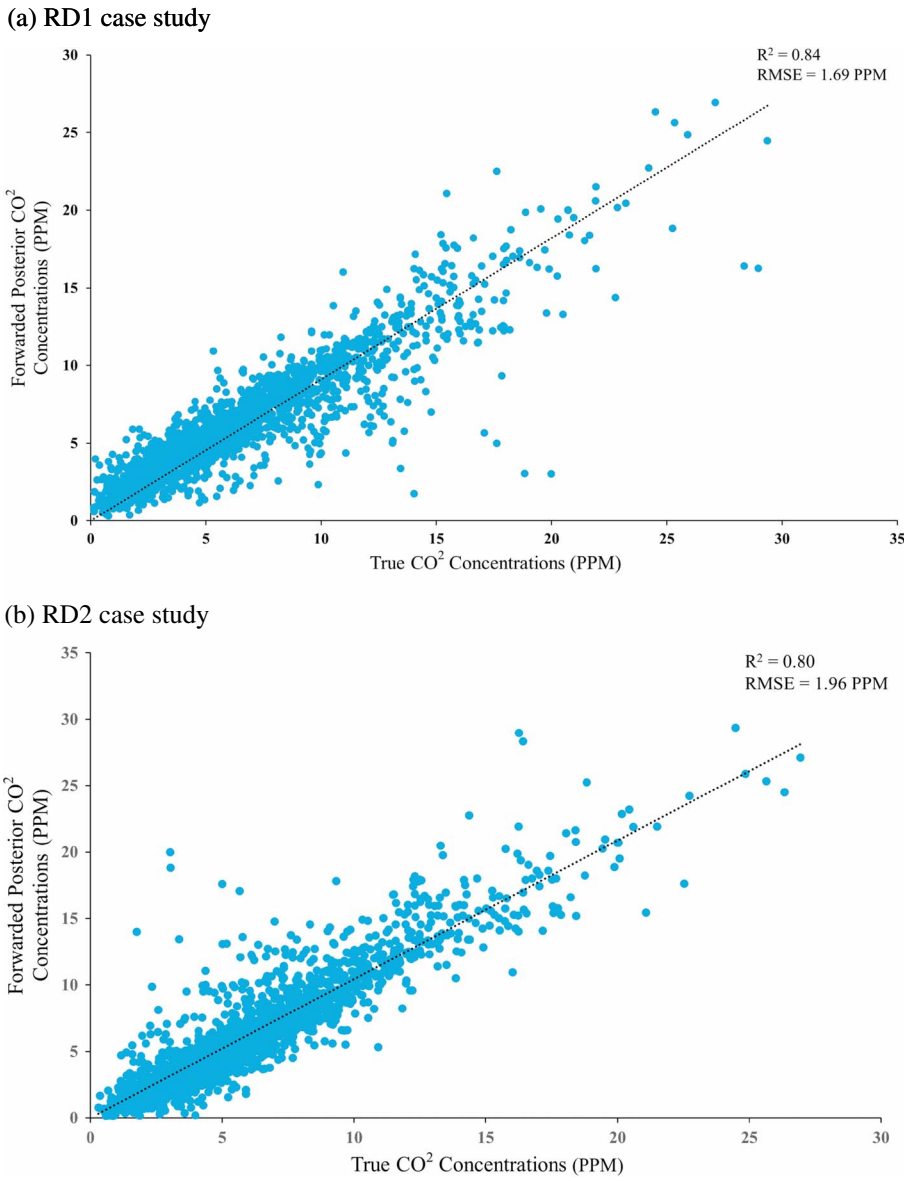

Figure A1. True and posterior concentration fits for (a) RD1 and (b) RD2 case studies.

References

Andrews, A. E., et al. (2015), CO_2, CO, and CH_4 measurements from tall towers in the NOAA Earth System Research Laboratory's Global Greenhouse Gas Reference Network: Instrumentation, uncertainty analysis, and recommendations for future high-accuracy greenhouse gas monitoring efforts, *Atmos. Meas. Tech.*, *7*, 647–687, doi:10.5194/amt-7-647-2014.

Brioude, J., et al. (2012), A new inversion method to calculate emission inventories without a prior at mesoscale: Application to the anthropogenic CO_2 emission from Houston, Texas, *J. Geophys. Res.*, *117*, D05312, doi:10.1029/2011JD016918.

Cambaliza, M., P. Shepson, D. Caulton, B. Stirm, D. Samarov, K. Gurney, J. Turnbull, K. Davis, A. Possolo, and A. Karion (2013), Assessment of uncertainties of an aircraft-based mass-balance approach for quantifying urban greenhouse gas emissions, *Atmos. Chem. Phys. Discuss.*, *13*, 29,895–29,945.

Department of Energy through the Ameriflux Management Project, the Midwestern Center of the National Institute for Global Environmental Change (NIGEC), the National Institute for Climate Change Research (NICCR), the Terrestrial Carbon Program (TCP), and the Terrestrial Ecosystem Sciences (TES) programs. CO_2 measurements at LJA were supported by the Scripps CO_2 program. We thank the following individuals for collecting and providing the atmospheric CO_2 data from the following sites: Arlyn Andrews (NOAA) for SNP, AMT, WBI, BAO, LEF, and WKT; Kirk Thoning (NOAA) for BRW; Mattew J. Parker (SRNL) for SCT; Marc Fischer (LBNL) and Arlyn Andrews (NOAA) for WGC; Kenneth Davis, Scott Richardson, and Natasha Miles (Pennsylvania State University) for CVA, OZA, KEW, CEN, MEA, ROL, and GAL; Britton Stephens (NCAR) and the Regional Atmospheric Continuous CO_2 Network in the Rocky Mountains (RACCOON) for NWR, SPL, and HDP; Beverly Law (Oregon State University) and the TERRA-PNW group for data from five Oregon sites, FIR, MET, YAH, MAP, and NGB; William Munger (Harvard University) and Steven Wofsy (Harvard University) for HFM; Doug Worthy (Environment Canada) for CDL, FRD, SBL, EGB, ETL, LLB, and CHM; Kimberly Novick (Indiana University) for MMS; Sebastien Biraud (LBNL) and Margaret Torn (LBNL) for SGP; and Ralph Keeling (Scripps Institution of Oceanography) and Lisa Welp (Purdue University) for LJA. Note that all the code required for evaluating, replicating, and building upon the results of this paper can be obtained without cost from Vineet Yadav by contacting him through email at vineet.yadav@jpl.nasa.gov. For obtaining the concentration data utilized in this study, researchers would have to directly (on their own) contact the principal investigators of towers listed above.

CIESIN (2012), National aggregates of geospatial data: Population, landscape and climate estimates version 3 (PLACE III), CIESIN, Columbia Univ., Palisades, N. Y. [Available at http://sedac.ciesin.columbia.edu/data/set/nagdc-population-landscape-climate-estimates-v3.]

Christen, A. (2014), Atmospheric measurement techniques to quantify greenhouse gas emissions from cities, *Urban Clim.*, *10*, 241–260.

Cressie, N. A. C. (1993), *Statistics for Spatial Data*, 928 pp., Wiley, New York.

Crisp, D., et al. (2004), The orbiting carbon observatory (OCO) mission, *Adv. Space Res.*, *34*(4), 700–709.

Dragoni, D., H. P. Schmid, C. S. B. Grimmond, and H. W. Loescher (2007), Uncertainty of annual net ecosystem productivity estimated using eddy covariance flux measurements, *J. Geophys. Res.*, *112*, D17102, doi:10.1029/2006JD008149.

Duren, R. M., and C. E. Miller (2012), Measuring the carbon emissions of megacities, *Nat. Clim. Change*, *2*(8), 560–562.

Elvidge, C. D., K. E. Baugh, E. A. Kihn, H. W. Kroehl, and E. R. Davis (1997), Mapping city lights with nighttime data from the DMSP Operational Linescan System, *Photogramm. Eng. Remote Sens.*, *63*(6), 727–734.

Fang, Y., A. Michalak, Y. Shiga, and V. Yadav (2014), Using atmospheric observations to evaluate the spatiotemporal variability of CO_2 fluxes simulated by terrestrial biospheric models, *Biogeosci. Discuss.*, *11*(6), 9215–9247.

George, K., L. H. Ziska, J. A. Bunce, and B. Quebedeaux (2007), Elevated atmospheric CO_2 concentration and temperature across an urban–rural transect, *Atmos. Environ.*, *41*(35), 7654–7665.

Gill, P. E., W. Murray, and M. H. Wright (1981), *Practical Optimization*, Academic Press, London, U. K.

Göckede, M., A. M. Michalak, D. Vickers, D. P. Turner, and B. E. Law (2010), Atmospheric inverse modeling to constrain regional scale CO_2 budgets at high spatial and temporal resolution, *J. Geophys. Res.*, *115*, D15113, doi:10.1029/2009JD012257.

Golub, G. H., and C. F. Van Loan (2012), *Matrix Computations*, 784 pp., John Hopkins Univ. Press, Baltimore, Md.

Gourdji, S. M., K. L. Mueller, K. Schaefer, and A. M. Michalak (2008), Global monthly averaged CO_2 fluxes recovered using a geostatistical inverse modeling approach: 2. Results including auxiliary environmental data, *J. Geophys. Res.*, *113*, D21115, doi:10.1029/2007JD009733.

Gourdji, S. M., A. Hirsch, K. Mueller, V. Yadav, A. Andrews, and A. Michalak (2010), Regional-scale geostatistical inverse modeling of North American CO_2 fluxes: A synthetic data study, *Atmos. Chem. Phys.*, *10*, 6151–6167.

Gourdji, S. M., K. L. Mueller, V. Yadav, D. N. Huntzinger, A. E. Andrews, M. Trudeau, G. Petron, T. Nehrkorn, J. Eluszkiewicz, and J. Henderson (2012), North American CO_2 exchange: Inter-comparison of modeled estimates with results from a fine-scale atmospheric inversion, *Biogeosciences*, *9*, 457–475.

Gratani, L., and L. Varone (2005), Daily and seasonal variation of CO_2 in the city of Rome in relationship with the traffic volume, *Atmos. Environ.*, *39*(14), 2619–2624.

Gurney, K. R., et al. (2002), Towards robust regional estimates of CO_2 sources and sinks using atmospheric transport models, *Nature*, *415*, 626–630.

Gurney, K. R., D. L. Mendoza, Y. Zhou, M. L. Fischer, C. C. Miller, S. Geethakumar, and S. de la Rue du Can (2009), High resolution fossil fuel combustion CO_2 emission fluxes for the United States, *Environ. Sci. Technol.*, *43*(14), 5535–5541.

Gurney, K. R., I. Razlivanov, Y. Song, Y. Zhou, B. Benes, and M. Abdul-Massih (2012), Quantification of fossil fuel CO_2 emissions on the building/street scale for a large U.S. City, *Environ. Sci. Technol.*, *46*(21), 12,194–12,202.

Huntzinger, D., W. M. Post, Y. Wei, A. Michalak, T. O. West, A. Jacobson, I. Baker, J. M. Chen, K. Davis, and D. Hayes (2012), North American Carbon Program (NACP) regional interim synthesis: Terrestrial biospheric model intercomparison, *Ecol. Modell.*, *232*, 144–157.

Idso, C. D., S. B. Idso, and R. C. Balling (2001), An intensive two-week study of an urban CO_2 dome in Phoenix, Arizona, USA, *Atmos. Environ.*, *35*(6), 995–1000.

Keeling, C. D., S. C. Piper, R. B. Bacastow, M. Wahlen, T. P. Whorf, M. Heimann, and H. A. Meijer (2005), Atmospheric CO_2 and $13CO_2$ exchange with the terrestrial biosphere and oceans from 1978 to 2000: observations and carbon cycle implications, in *A History of Atmospheric CO_2 and its effects on Plants, Animals, and Ecosystems*, edited by J. R. Ehleringer, T. E. Cerling, and M. D. Dearing, pp. 83–113, Springer, New York.

Kitanidis, P. K. (1995), Quasi-linear geostatistical theory for inversing, *Water Resour. Res.*, *31*, 2411–2419, doi:10.1029/95WR01945.

Kort, E. A., C. Frankenberg, C. E. Miller, and T. Oda (2012), Space-based observations of megacity carbon dioxide, *Geophys. Res. Lett.*, *39*, L17806, doi:10.1029/2012GL052738.

Kuai, L., et al. (2013), Profiling tropospheric CO_2 using Aura TES and TCCON instruments, *Atmos. Meas. Tech.*, *6*, 63–79, doi:10.5194/amt-6-63-2013.

Kulawik, S. S., et al. (2013), Comparison of improved Aura Tropospheric Emission Spectrometer CO_2 with HIPPO and SGP aircraft profile measurements, *Atmos. Chem. Phys.*, *13*, 3205–3225, doi:10.5194/acp-13-3205-2013.

Lauvaux, T., N. L. Miles, S. J. Richardson, A. Deng, D. R. Stauffer, K. J. Davis, G. Jacobson, C. Rella, G.-P. Calonder, and P. L. DeCola (2013), Urban emissions of CO_2 from Davos, Switzerland: The first real-time monitoring system using an atmospheric inversion technique, *J. Appl. Meteorol. Climatol.*, *52*(12), 2654–2668.

Lin, J. C., C. Gerbig, S. C. Wofsy, A. E. Andrews, B. C. Daube, K. J. Davis, and C. A. Grainger (2003), A near-field tool for simulating the upstream influence of atmospheric observations: The Stochastic Time-Inverted Lagrangian Transport (STILT) model, *J. Geophys. Res.*, *108*(D16), 4493, doi:10.1029/2002JD003161.

Matese, A., B. Gioli, F. Vaccari, A. Zaldei, and F. Miglietta (2009), Carbon dioxide emissions of the city center of Firenze, Italy: Measurement, evaluation, and source partitioning, *J. Appl. Meteorol. Climatol.*, *48*(9), 1940–1947.

Mays, K. L., P. B. Shepson, B. H. Stirm, A. Karion, C. Sweeney, and K. R. Gurney (2009), Aircraft-based measurements of the carbon footprint of Indianapolis, *Environ. Sci. Technol.*, *43*(20), 7816–7823.

Menke, W. (2012), *Geophysical Data Analysis: Discrete Inverse Theory*, vol. 45, Academic Press, Palisades, New York.

McKain, K., S. Wofsy, T. Nehrkorn, J. Eluszkiewicz, J. R. Ehrlinger, and B. B. Stephens (2012), Assessment of ground-based atmospheric observations for verification of greenhouse gas emissions from an urban region, *Proc. Natl. Acad. Sci. U.S.A.*, *109*, 8423–8428.

Michalak, A. M., and P. K. Kitanidis (2003), A method for enforcing parameter nonnegativity in Bayesian inverse problems with an application to contaminant source identification, *Water Resour. Res.*, *39*(2), 1033, doi:10.1029/2002WR001480.

Michalak, A. M., L. Bruhwiler, and P. P. Tans (2004), A geostatistical approach to surface flux estimation of atmospheric trace gases, *J. Geophys. Res.*, *109*, D14109, doi:10.1029/2003JD004422.

Miller, J. B., et al. (2012), Linking emissions of fossil fuel CO_2 and other anthropogenic trace gases using atmospheric $^{14}CO_2$, *J. Geophys. Res.*, *117*, D08302, doi:10.1029/2011JD017048.

Miller, S. M., A. M. Michalak, and P. J. Levi (2014), Atmospheric inverse modeling with known physical bounds: An example from trace gas emissions, *Geosci. Model Dev.*, *7*(1), 303–315.

Miteva, B. (2002), *Atlas of the Biosphere: Built-Up Land*, edited by N. I. f. E. Studies, Univ. of Wisconsin, Madison.

Newman, S., X. Xu, H. P. Affek, E. Stolper, and S. Epstein (2008), Changes in mixing ratio and isotopic composition of CO_2 in urban air from the Los Angeles basin, California, between 1972 and 2003, *J. Geophys. Res.*, *113*, D23304, doi:10.1029/2008JD009999.

Oda, T., and S. Maksyutov (2011), A very high-resolution (1 km × 1 km) global fossil fuel CO_2 emission inventory derived using a point source database and satellite observations of nighttime lights, *Atmos. Chem. Phys.*, *11*(2), 543–556.

Olsen, S. C., and J. T. Randerson (2004), Differences between surface and column atmospheric CO_2 and implications for carbon cycle research, *J. Geophys. Res.*, *109*, D02301, doi:10.1029/2003JD003968.
Pacala, S., et al. (2010), *Verifying Greenhouse Gas Emissions: Methods to Support International Climate Agreements*, *Natl. Res. Counc. Rep.*, 124 pp., Comm. on Methods for Estim. Greenhouse Gas Emiss., The Natl. Acad. Press, Washington, D. C.
Randerson, J. T., M. V. Thompson, T. J. Conway, I. Y. Fung, and C. B. Field (1997), The contribution of terrestrial sources and sinks to trends in the seasonal cycle of atmospheric carbon dioxide, *Global Biogeochem. Cycles*, *11*, 535–560, doi:10.1029/97GB02268.
Ray, J., V. Yadav, A. M. Michalak, B. van Bloemen Waanders, and S. A. Mckenna (2014a), A multiresolution spatial parameterization for the estimation of fossil-fuel carbon dioxide emissions via atmospheric inversions, *Geosci. Model Dev.*, *7*(5), 1901–1918, doi:10.5194/gmdd-7-1277-2014.
Ray, J., J. Lee, V. Yadav, S. Lefantzi, A. M. Michalak, and B. van Bloemen Waanders (2014b), A sparse reconstruction method for the estimation of multiresolution emission fields via atmospheric inversion, *Geosci. Model Dev. Discuss.*, *7*(4), 5623–5659, doi:10.5194/gmdd-7-5623-2014.
Rayner, P. J., I. G. Enting, R. J. Francey, and R. Langenfelds (1999), Reconstructing the recent carbon cycle from atmospheric CO_2, delta13C and O_2/N_2 observations, *Tellus, Ser. B*, *51*(2), 213–232.
Reid, K., and D. Steyn (1997), Diurnal variations of boundary-layer carbon dioxide in a coastal city-observations and comparison with model results, *Atmos. Environ.*, *31*(18), 3101–3114.
Rice, A., and G. Bostrom (2011), Measurements of carbon dioxide in an Oregon metropolitan region, *Atmos. Environ.*, *45*(5), 1138–1144.
Richardson, S. J., N. L. Miles, K. J. Davis, E. R. Crosson, C. W. Rella, and A. E. Andrews (2012), Field testing of cavity ring-down spectroscopy analyzers measuring carbon dioxide and water vapor, *J. Atmos. Oceanic Technol.*, *29*, 397–406, doi:10.1175/JTECH-D-11-00063.1.
Rigby, M., R. Toumi, R. Fisher, D. Lowry, and E. G. Nisbet (2008), First continuous measurements of CO_2 mixing ratio in central London using a compact diffusion probe, *Atmos. Environ.*, *42*(39), 8943–8953.
Rodell, M., P. Houser, U. Jambor, J. Gottschalck, K. Mitchell, C.-J. Meng, K. Arsenault, B. Cosgrove, J. Radakovich, and M. Bosilovich (2004), The global land data assimilation system, *Bull. Am. Meteorol. Soc.*, *85*(3), 381–394, doi:10.1175/BAMS-85-3-381.
Schmid, H. P., C. S. B. Grimmond, F. Cropley, B. Offerle, and H. B. Su (2000). Measurements of CO_2 and energy fluxes over a mixed hardwood forest in the mid-western United States, *Agric. For. Meteorol.*, *103*(4), 357-374.
Schneider, A., M. A. Friedl, and D. Potere (2009), A new map of global urban extent from MODIS satellite data, *Environ. Res. Lett.*, *4*(4), 044003.
Schwarz, G. (1978), Estimating the dimension of a model, *Ann. Stat.*, *6*(2), 461–464.
Shiga, Y. P., A. M. Michalak, S. M. Gourdji, K. L. Mueller, and V. Yadav (2014), Detecting fossil fuel emissions patterns from sub-continental regions using North American in-situ CO_2 measurements, *Geophys. Res. Lett.*, *41*, 4381–4388, doi:10.1002/2014GL059684.
Sloop, C., and E. Novakovskaia (2012), Data from the dense atmospheric observing network to detect GHG trends and anomalies, paper presented at WMO Technical Conference on Meteorological and Environmental Instruments and Methods of Observation, TECO–2012.
Stephens, B. B., N. L. Miles, S. J. Richardson, S. Watt, and K. J. Davis (2011), Atmospheric CO_2 monitoring with single-cell NDIR-based analyzers, *Atmos. Meas. Tech.*, *4*, 2737–2748, doi:10.5194/amt-4-2737-2011.
Strong, C., C. Stwertka, D. Bowling, B. Stephens, and J. Ehleringer (2011), Urban carbon dioxide cycles within the Salt Lake Valley: A multiple-box model validated by observations, *J. Geophys. Res.*, *116*, D15307, doi:10.1029/2011JD015693.
Tans, P. P., I. Y. Fung, and T. Takahashi (1990), Observational constraints on the global atmospheric CO_2 budget, *Science*, *247*(4949), 1431–1438.
Turnbull, J. C., et al. (2015), Toward quantification and source sector identification of fossil fuel CO_2 emissions from an urban area: Results from the INFLUX experiment, *J. Geophys. Res. Atmos.*, *120*, 292–312, doi:10.1002/2014JD022555.
Urbanski, S., C. Barford, S. Wofsy, C. Kucharik, E. Pyle, J. Budney, K. McKain, D. Fitzjarrald, M. Czikowsky, and J. W. Munger (2007), Factors controlling CO_2 exchange on timescales from hourly to decadal at Harvard Forest, *J. Geophys. Res.*, *112*, G02020, doi:10.1029/2006JG000293.
van der Werf, G. R., J. T. Randerson, L. Giglio, G. J. Collatz, P. S. Kasibhatla, and J. A. F. Arellano (2006), Interannual variability in global biomass burning emissions from 1997 to 2004, *Atmos. Chem. Phys.*, *6*, 3423–3441.
Velazco, V. A., M. Buchwitz, H. Bovensmann, M. Reuter, O. Schneising, J. Heymann, T. Krings, K. Gerilowski, and J. P. Burrows (2011), Towards space based verification of CO_2 emissions from strong localized sources: Fossil fuel power plant emissions as seen by a CarbonSat constellation, *Atmos. Meas. Tech.*, *4*(12), 2809–2822.
Vogel, F. R., B. Tiruchittampalam, J. Theloke, R. Kretschmer, C. Gerbig, S. Hammer, and I. Levin (2013), Can we evaluate a fine-grained emission model using high-resolution atmospheric transport modelling and regional fossil fuel CO_2 observations?, *Tellus, Ser. B*, *65*, 18681.
Yadav, V., and A. M. Michalak (2013), Improving computational efficiency in large linear inverse problems: An example from carbon dioxide flux estimation, *Geosci. Model Dev.*, *6*, 583–590, doi:10.5194/gmd-6-583-2013.
Yadav, V., K. L. Mueller, and A. M. Michalak (2013), A backward elimination discrete optimization algorithm for model selection in spatio-temporal regression models, *Environ. Modell. Software*, *42*, 88–98.
Zimnoch, M., J. Godlowska, J. Necki, and K. Rozanski (2010), Assessing surface fluxes of CO_2 and CH_4 in urban environment: A reconnaissance study in Krakow, Southern Poland, *Tellus, Ser. B*, *62*(5), 573–580.